Analysis of Progressive Tensile Damage of Multi-walled Carbon Nanotube Reinforced Carbon Fiber Composites by Using Acoustic Emission and Micro-CT

Ning Pei[1,2] · Junjun Shang[3] · Leonard J. Bond[4]

Abstract

The potential to provide improved performance for advanced composites through the addition of multi-walled carbon nanotubes (MWCNTs) to carbon fiber composites is of interest in several applications. To investigate performance four types of composite specimens with different off-axis angles were subjected to progressive tensile loading. The results show that MWCNTs can improve the bearing capacity of the composite and the off-axis orientation angle can enhance the toughness of the composite. During loading acoustic emission (AE) signals were collected and they were post-processed using cluster analysis based on a Fuzzy C-Means algorithm. The analysis of the AE signals shows that data can be divided into categories which correlate with three damage modes: matrix cracking, fiber debonding and fiber breakage. The AE peak frequency characteristics of each damage mode were identified. Additional characterization was provided by using micro-computed tomography (Micro-CT) during the progressive tensile loading process. The CT images visualize damage location and evolution in the composites and data exhibit good correlations with the AE data for defects predication. The combination of AE and micro-CT technology were shown to effectively characterize damage evolution of the composites, and such data can potentially serve as a reference for the structural health monitoring of these composites when used in structures.

1 Introduction

Carbon fiber-reinforced polymer (CFRP) composites have the advantage of higher stiffness-to-weight ratio and better fatigue performance when compared to metals typically used in aircraft structural components. CFRP has been widely used in industry, especially for aerospace applications, such as for the Boeing 787. Advanced composites can make up approximately 50% by weight in modern commercial aircraft [1], and most of this material is in the form of laminates.

When using CFRP composites in the form of laminates during service various forms of degradation and damage can occur. With these materials typical defects can be in the form of matrix cracks and fiber dis-bonding [2, 3]. To improve material performance efforts have been made to modify the composition and the manufacturing process so as to enhance the mechanical properties of the composite laminates and prevent or at least limit the formation of defects. One approach to improving performance is the addition of multi-walled carbon nanotubes (MWCNTs), one of the strongest and stiffest materials that exist, which can be incorporated into the polymer matrix to improve the composites strength [4–6]. Various groups have investigated the properties of these material. Tarfaoui et al. [7] studied delamination progression in carbon nanotubes (CNTs) reinforced composite laminates during short beam shear tests. The CNT mass fractions for the materials ranged from 0 to 4%. To assess the failure behavior, failure modes and the delamination which occurs the materials were characterized

✉ Leonard J. Bond
  bondlj@iastate.edu

1 School of Mechanical Engineering, Beijing Institute of Technology, Beijing 100081, China

2 Key Laboratory of Fundamental Science for Advanced Machining, Beijing Institute of Technology, Beijing 100081, China

3 Faculty of Materials and Manufacturing, Beijing University of Technology, Beijing 100124, China

4 Department of Aerospace Engineering & Center for Nondestructive Evaluation, Iowa State University, Ames, IA 50010, USA

using a scanning electron microscopy and high resolution optical (Kayence) microscopy. This study demonstrated that a small amount of CNTs used as additives can enhance the interfacial resistance and causes a delay in the occurrence of delamination. Furthermore, El Moumen et al. [8] used micro-indentation with forces ranging from 1 mN to 10 N to determine the elastic mechanical properties of MWCNT reinforced polymer composites. The reinforced polymer composites exhibited improved mechanical properties, with the rigidity of the nanotube modified polymer composites significantly improved (about 3.5%) by adding only 1% of CNT. The results illustrated that adding relatively small amounts of MWCNTs can improve the fracture interfacial rigidity and can slow micro-crack evolution.

The issue then becomes to provide tools that can be used to investigate aging and degradation of MWCNT materials, so as to better understand in-service performance of these advanced composites. Acoustic emission (AE) technology has also been widely used as an effective structure health monitoring (SHM) method in composite damage research [9–11] and this was investigated.

For AE as a monitoring technique, there can be energy release during a damage process, where the energy will spread as elastic waves which can be detected using piezo-electric material based sensors. By analyzing the received AE signals, a relationship can potentially be established between the AE signals and different kinds of damage, which can help to develop the understanding of the damage mechanics of the composites and also provide guidance for industry applications. Njuhovic et al. [12] adopted AE technology to investigate interface failure mechanisms of metallized glass fiber reinforced epoxy composites which were pre-treated with Aluminium oxide (Al_2O_3). Measurements were made where the AE signals from the coating-substrate system were recorded during peel testing to characterize interfacial failure. It was shown that the absolute AE-energy was sensitive to changes in the surface topography and therefore peel strength. Furthermore, Munoz et al. [13] combined AE and infrared thermography (IRT) technology to study damage evolution in carbon fiber reinforced composites under tensile loads. When using spatial and time analysis of the acoustic events and heat sources, some correlations between the amplitude of AE signals and IRT data were identified.

In investigating AE signal analysis, some researchers applied an unsupervised pattern recognition procedure to identify damage mechanisms from the features seen in the acoustic signals. Li et al. [14] utilized cluster analysis based on a k-means + + algorithm to analyze the AE signals from tensile tests on carbon fiber/epoxy composites. Two important features, the frequency and peak amplitude, were found to be dominant in cluster analysis. Cluster bounds were identified for different failure modes. These results can be used as a reference for AE analysis of other carbon fiber/epoxy

composites. Similarly, Monti et al. [15] discussed mechanical behavior of composites consisting of a thermoplastic matrix reinforced by flax fibers under uniaxial tensile loading. The appearance and evolution of damage mechanisms were detected and followed by using data given with AE technology. According to the analysis of AE events post-processed by the k-means algorithm, three or four classes of events were observed. A correlation between these AE event classes and the observed damage mechanisms was then proposed. Zhao et al. [16] proposed an approach based on a Fuzzy C-Means (FCM) algorithm to process the AE signals collected during tensile tests on composites. The results showed that there are in general three failure mechanisms in the tensile process for carbon/glass fiber reinforced hybrid woven composites and these can be described as matrix cracking, fiber debonding and fiber breakage. Similarly, the cluster bound of each damage mode was also found. It is seen with these data that cluster analysis is an effective tool to apply to multi-parametrical AE signals and to provide pattern recognition applied to AE data given by the composite damage process.

To provide additional insights into internal defect and the damage process of composite laminates, micro-computed tomography (Micro-CT) technology can be applied to obtain detailed 3D images of local features inside the composites [17–19]. Micro-CT can effectively reconstruct the internal structure of CFRP and it has been widely applied. Zhang et al. [20] investigated the influence of different off-axis angles on the shear progressive damage of three-dimensional (3D) woven carbon/epoxy composites under short beam shear loads. The internal damage initiation/evolution of 3D woven composites was characterized using a Micro-CT technique. The results show that the off-axis angles used had significant influence on the resulting mechanical behavior, damage evolution and final failure mechanisms. Li et al. [21] used synchrotron radiation computer tomography (SRCT) to observe the failure process of 3D woven carbon-fiber reinforced composites. The method could record the images of 3D crack initiation and propagation. From analysis of the experimental results, it could be concluded that with the increase in the braiding angle, the out-plane tension strength increased but the out-plane shear strength decreased.

Recently a few studies have been performed to investigate the mechanical properties of MWCNTs reinforced CFRP composite laminates [22–25]. There has also been limited work to investigate the damage response of polymer composite reinforced with CNTs/carbon fibers [4, 26]. From reviewing the literature it appears that the effect of variations in the off-axis angle on the progression of damage in MWC-NTs reinforced CFRP laminates is not well understood. In this article, progressive tensile tests for MWCNTs reinforced composites with different off-axis angles were monitored using AE technology. A cluster analysis based on the FCM

algorithm was used to analyze the AE signals obtained during the tensile testing process for the specimens. In addition, 3D reconstruction of the damage to the CFRP during the tensile tests was performed using Micro-CT technology, which gave a method to observe internal defects.

## 2 Specimen Preparation and Test Methods

2.1 Materials and Specimens

Four types of CFRP specimens were prepared with 10 layers of orthogonal plain-weave carbon fiber. Figure 1 shows the structure for the four different CFRP laminates which were fabricated. The epoxy resin was poured into a beaker and mixed until uniform when it was ready for use. The appropriate amount of acetone and MWCNTs with 0.5wt% of epoxy resin [8] were added to the beaker and stirred until uniformly mixed. The curing agent was added after the acetone in the mixed liquid has completely evaporated. The mass ratio between the epoxy resin and the curing agent is 3:1.

The CFRP laminates were then manufactured by using a vacuum assisted resin infusion (VARI) method. This method ensures that the MWCNTs disperse homogeneously between every single carbon fiber layer. The as-prepared CFRP laminates were cured for 48 h at room temperature (20℃). Afterward, the laminates were put in a drying oven for 8 h at 100℃. After removal and allowing them to cool to the room temperature, the CFRP laminates with the thickness (T) of 2.5 ± 0.1 mm were cut into specimens with the size of 100 mm × 25 mm (Fig. 1e).

In order to study the influence of the off-axis angle on the properties of the composite materials, the axial angles for Specimen B, C and D are fabricated as 0°, 30° and 45°, respectively. Meanwhile, specimen A, which was used as a reference was fabricated using the same method but without MWCNTs. The axial angles for specimen A is fabricated as 0°, with the aim to enable the effect of MWCNTs on the mechanical property for the composites to be studied. In order to increase the contact force, so as to avoid a sample falling off from clamps, two pieces of aluminum sheets were glued on both ends of the specimens. The structure of the materials with different axial angles and morphology features for specimens A, B, C and D are as shown in Fig. 1a–d. Figure 1e shows the side view of the sample, where the aluminum sheets are represented by the four black rectangles. In addition to different structures three specimens in each class of composite materials were fabricated.
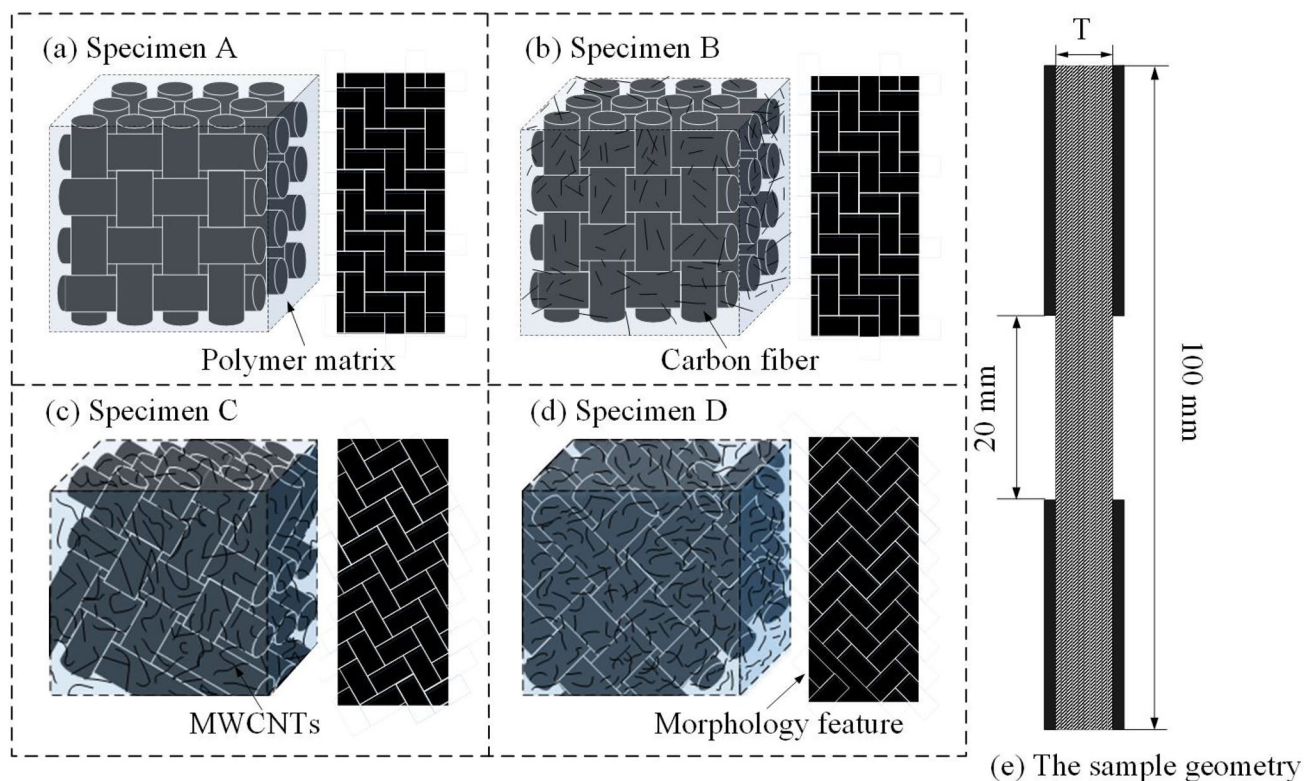
Fig. 1 Schematic shown the structure with different off-axis angles and morphology features for samples: **a** A, **b** B, **c** C and **d** D, respectively. **e** shows the sample geometry

2.2 Tensile Testing and Monitoring

The tensile tests of the composite specimens were performed with a crosshead speed of 1 mm/min using a tensile testing machine (CSS-1110, with maximum load 100 KN) and the damage evolution process was monitored using an AE system (Express-8, Physical Acoustic Corporation) in real time. One wideband AE sensor (RS-54A) with frequency range of 100–900 kHz was mounted on the specimen surface with silicone grease used as the couplant and tape to hold it in place. A preamplifier with gain of 40 dB was used to enhance the measured signal monitored during the tensile testing. The typical AE experiment system and typical parameters of AE signal are shown in Fig. 2.

2.3 Cluster Analysis Methods

The FCM method has been applied for analyzing the received AE data. Compared to the commonly-used cluster arithmetic approaches like K-means and K-means + + methods, the biggest difference for the FCM method is the introduction of fuzzy concepts and making it a soft-clustering method. Each input vector is no longer subordinate to a specific cluster, but is represented by its membership degree, which can better determine the critical value for different categories compared with the K-means and K-means + + methods. Assuming that $X=\{x_1, x_2, \cdots, x_n\}$ is a finite data set in feature space R^n, X can be divided into C ($2 \leqslant C \leqslant n$) categories, and C cluster centers can be written as $V=\{v_1, v_2, \cdots, v_n\}$. The objective function method and the corresponding constraint condition of the Fuzzy C-Means (FCM) can be written as [27, 28]:

$$J = \sum_{i=1}^{n} \sum_{j=1}^{c} u_{ij}^{m} \left\| x_i - v_j \right\|^2 \tag{1}$$

$$\sum_{i=1}^{c} u_{ij} = 1, j = 1, 2 \cdots, n \tag{2}$$

where c, n are the numbers of clusters and data samples; m is a weighting exponent applied to distinguish family members, and $m \in [1, \infty]$. The objective function J represents the sum of the squares of the distances from the feature points to the cluster center, and the clustering problem is then to make the objective function reach the minimum value.

2.4 Micro-CT 3D Image Construction

Micro-CT 3D images can then be used for identifying the characteristics (including location, type and size) of possible defects inside the specimen. For this research a ZEISS Xradia 520 Versa system was used for the measurements. The main principle of the system is to obtain the gray-scale projection containing structure information based on the X-ray absorption contrast difference for different structures of the measured sample [29, 30]. This system is composed of the X-ray source (30–160 kV), sample table and detector (including scintillator screen, high-resolution detector optics and CCD camera), as shown in Fig. 3.
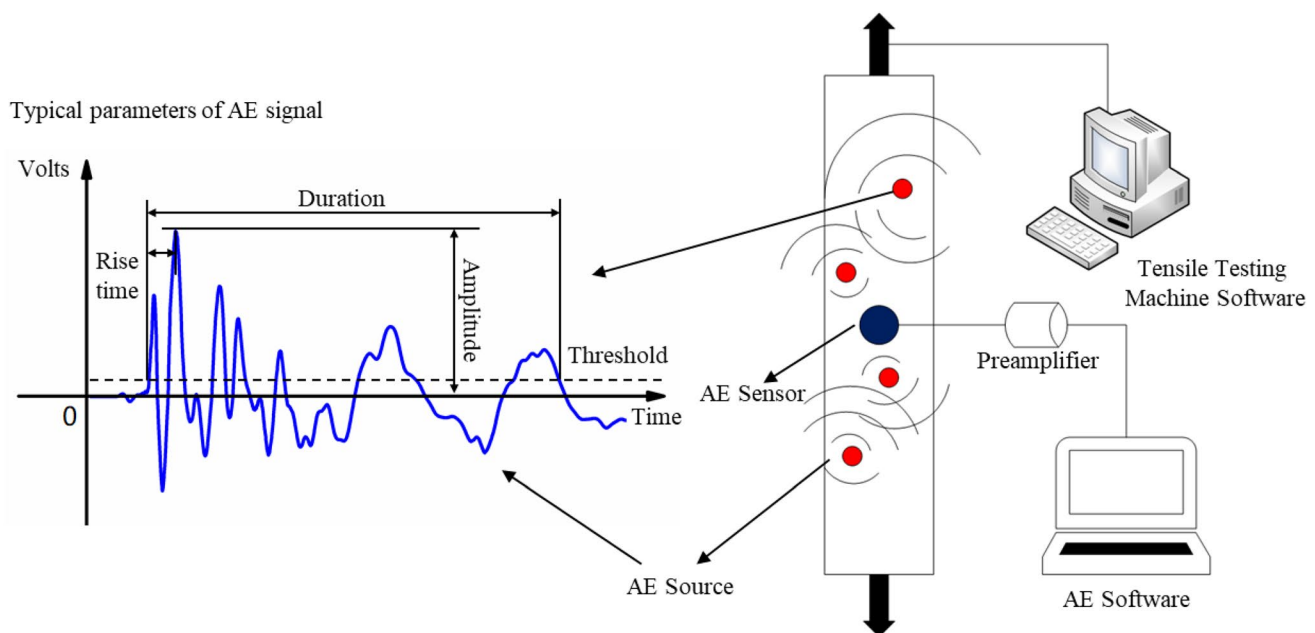
Fig. 2 Schematic showing the AE experiment system and typical parameters monitored for the AE signal
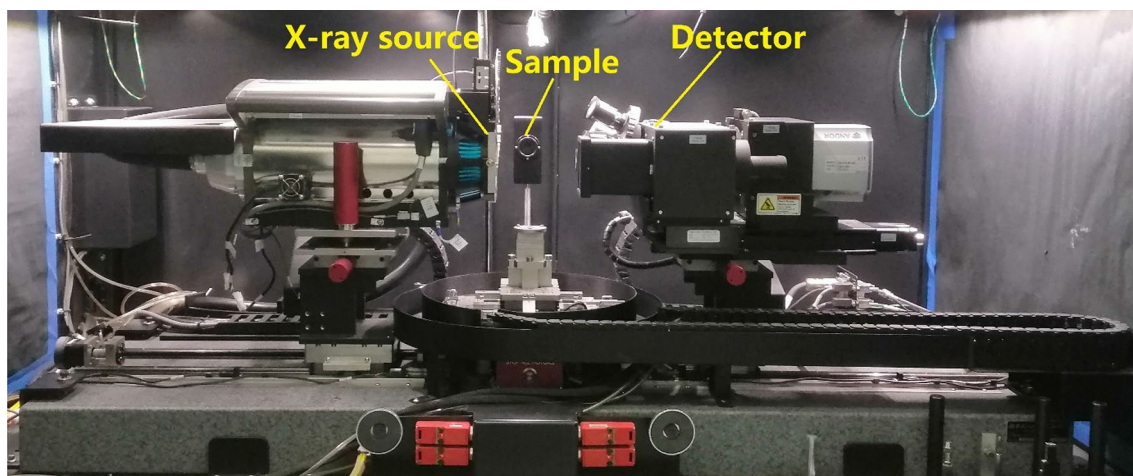
Fig. 3 Photograph showing the basic structure of the 3D X-ray imaging system

For the measurement, the excitation voltage of 60 kV and the source power of 5.0 W were used. The distance between the source and the measuring samples was set to 60 mm, while the distance from the sample to the detector is 140 mm. For these settings, a voxel size of 20 µm can be reached with the 0.4X objective, for the sample size $100 \times 25 \times 2.5$ mm. For each sample, it requires about 2 h for measurement and to process data to form a 3D image.

3 Results and Discussion

3.1 Mechanical Properties of Composite Specimens

Examples of the load–displacement curves for each of the 4 types of composite specimen are shown in Fig. 4.

The ultimate loads of the composite specimens were obtained from a series of tensile tests. The average failure load of specimens A, B, C and D are 23.8, 29.7, 11.2 and 8.4 kN, respectively. When the load curves are compared for specimen A and B, the failure load is larger and the stiffness (the slope of the load–displacement curve) of specimen B is higher than that of specimen A. These data demonstrate that a small amount of MWCNTs added to the material can

Fig. 4 The tensile loading curve versus displacement for each of the 4 types of composite specimens (Color figure online)
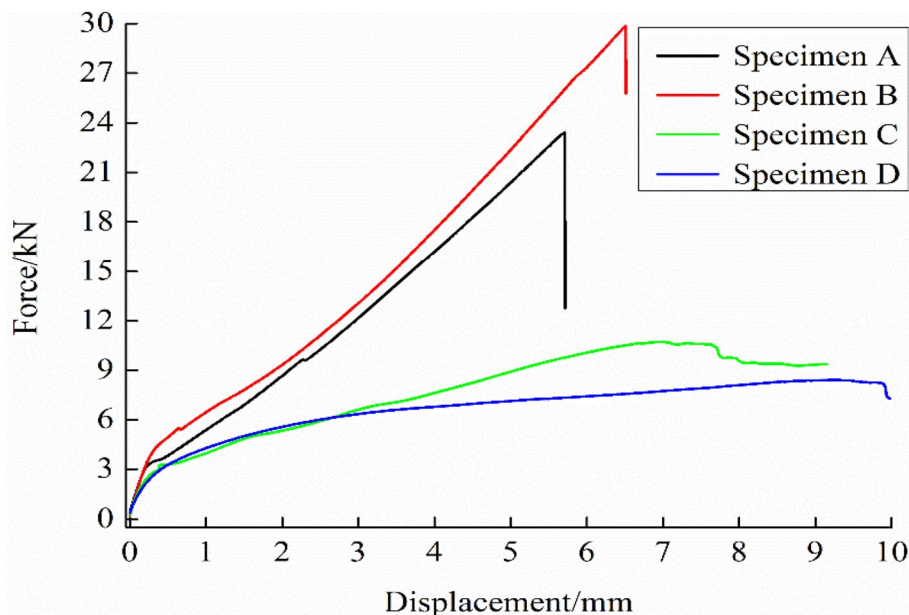
improve the mechanical properties of the composites, which is consist with the conclusion previously reported in the literature [7, 25].

From analyzing the load–displacement curves of specimen A, B, C and D, it was seen that as the material off-axis angle orientation increases this reduces the carrying capacity of the composites, even with nominally the same composition. As the off-axis angle increasing, the failure load decreases. For specimens of type A and B, with the tensile load increasing the load curve increases linearly, and during the tensile test there was no obvious deformation seen in specimens A and B when observed with the naked eyes. When the load increases up to the breaking point, there are sudden fractur failures which can be observed on the load–displacement curves. Nevertheless, for specimens type C and D, with the load increase the slope of the curve (which represents the stiffness of the material) decreases and there are gradually transitions to nonlinearity. It is also observed during the test that when the load increased to about 8 kN, obvious deformation can be seen with specimen type C. Similar deformation is seen when the load reaches about 5.4 kN for specimen type D. For specimens type C and D, when the load increases up to the maximum load, they underwent deformation rather than fracture, which is different from what is seen with specimens type A and B. What's more, it is also obvious that when the specimen fails, the deformation of specimens type C and D is significantly larger than that of specimens type A and B, which seems to imply that the off-axis structural morphology can improve the toughness of the composite.

3.2 Characteristics of the AE Signals

During the tensile tests the AE system was used to record the received signal, which was then used for analyzing the damage evolution mechanism. With the aim to study how the off-axis angle morphology influences the progressive tensile damage for MWCNTs reinforced carbon fiber composites, AE signals analysis was applied to data from specimens of type B, C and D respectively.

The AE amplitude and cumulative hits versus time for the typical composite specimens is shown in Fig. 5. For specimens type B, initially few AE signals are generated and the cumulative hits rises slowly, which can be seen from Fig. 5a. This result indicates that the specimen, at this time, is less damaged. With the increase of the tensile load, the damage of the specimen is continuously intensified. Therefore, a large number of AE signals are generated and the increasing rate of the cumulative hits continues to accelerate, as the load is increased. Before the failure load is reached, the rate of cumulative hits reaches a peak. However, for specimens type C and D, it can be seen from the data in Fig. 5b and c that in the middle of the tensile test, the increase in the rate
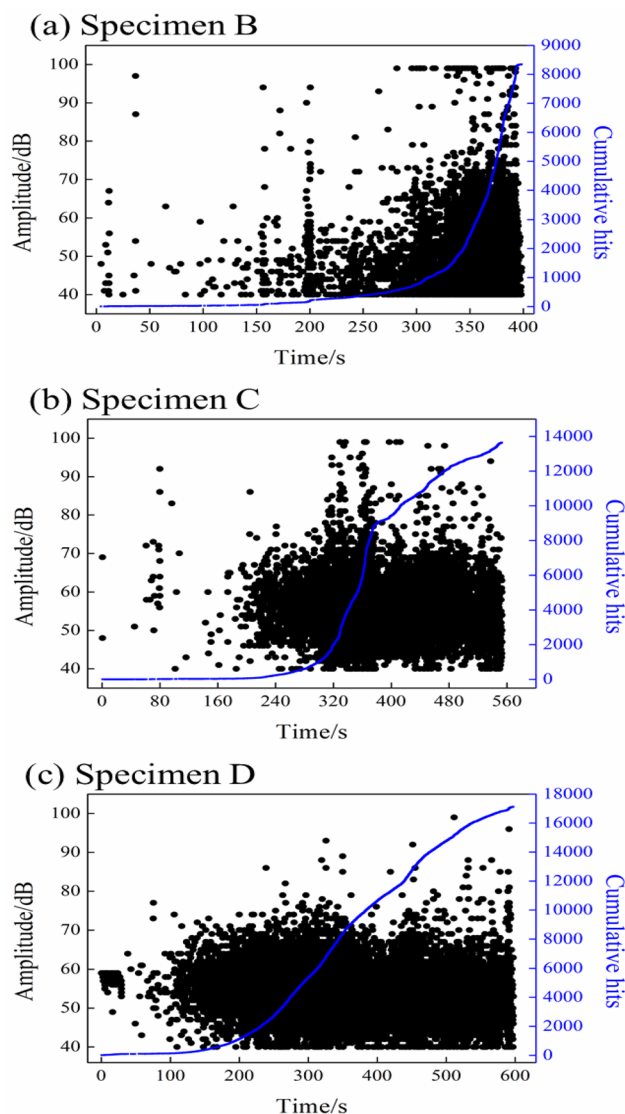
Fig. 5 AE amplitude and cumulative hits versus time for **a** specimen B, **b** specimen C and **c** specimen D, respectively

of the cumulative hits reaches a maximum, which is due to the deformation of the specimen during the tensile process rather than a sudden fracture, which is seen with a specimen of type B.

When the stiffness data are considered it is seen that values for specimens type C and D are lower than specimen type B, which can lead to a longer duration of failure and a larger number of cumulative hits. The cumulative hits recorded for specimen type B was between 8000 and 9000, for specimen type C and D close to 14,000 and 18,000 respectively, as is shown in Fig. 5. It seems that with the single parameter characterization of AE the signals it is hard to fully describe the damage behavior. To provide additional insights with the AE signals there was a need to process data with a multi-parameter analysis [14–16].

3.3 Cluster Analysis of AE Signals

AE signals typically have several characteristic parameters including amplitude, rise time, duration, counts, peak frequency (PF), RA value (rise time divided by peak amplitude), and centroid frequency (CF) which are used. Three

Fig. 6 Three clusters separated by the peak amplitude and peak frequency for **a** specimen type B, **b** specimen type C and **c** specimen type D, respectively
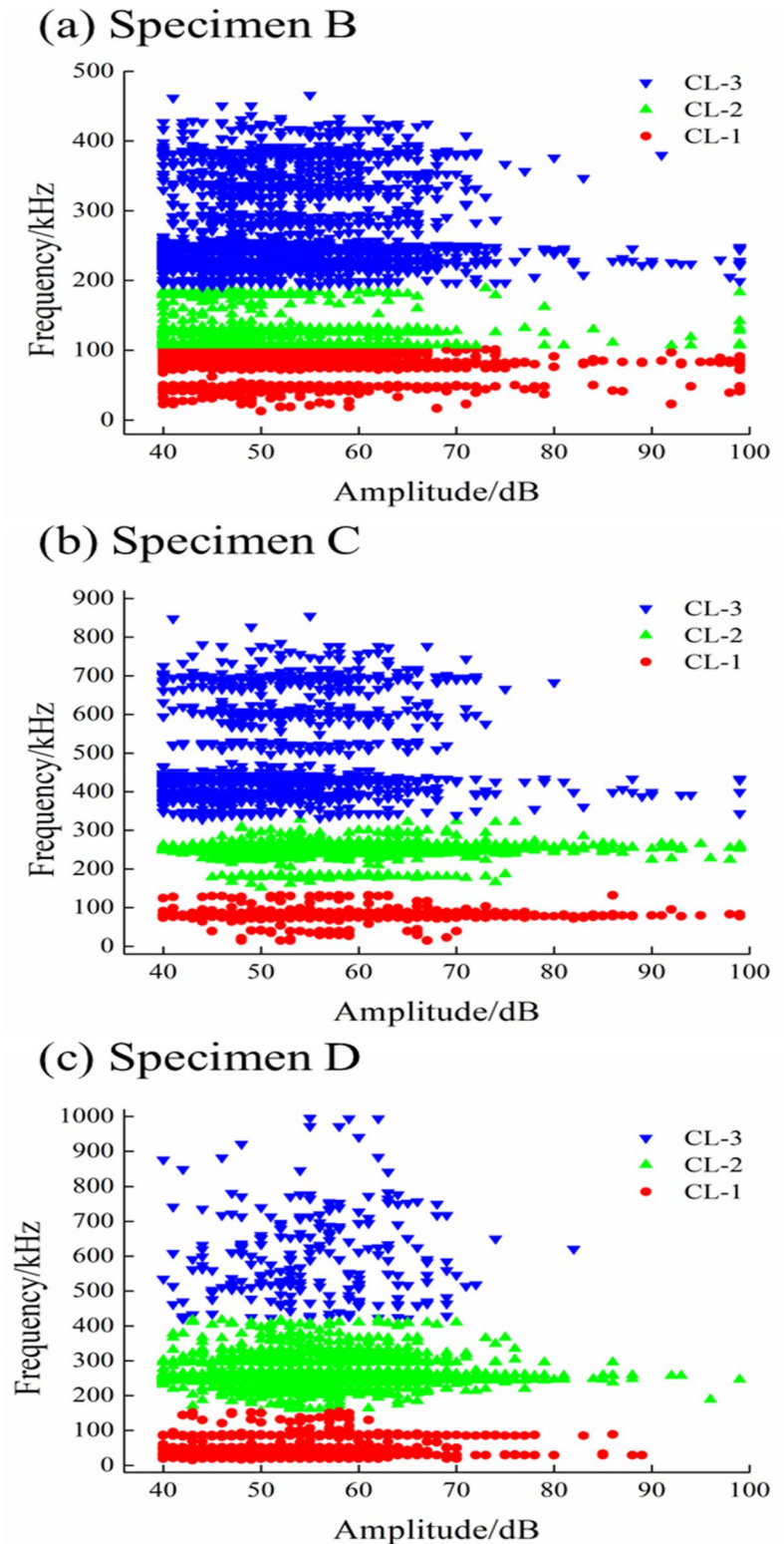
of them, the amplitude, PF and RA value, are selected to be used in a cluster analysis of AE signals based on use of the FCM algorithm [16]. Meanwhile, amplitude and PF which are important characteristic parameters are also selected to analyze the AE signals [14, 16]. With reference to other studies of composite material damage [15, 16, 31], it is found that in general, common composite damage includes three types: matrix cracking, fiber debonding, and fiber breaking. Therefore, the cluster number for AE signals was chosen to be three. In analyzing the data shown in Fig. 6 this shows that three clusters referred to as CL-1, CL-2 and CL-3 are separated by amplitude and peak frequency. According to the statistical analysis of the AE signals for each cluster shown in Fig. 6a–c, cluster bounds for every type of specimen and the number of AE signals is obtained and shown in Table 1.

For data for specimen type B shown in Fig. 6a, CL-1 has a low peak frequency of below 105 kHz. CL-2 has a peak frequency in the range of 107–189 kHz. CL-3 has a peak frequency over 191 kHz. For data for specimen type C shown in Fig. 6b, the amplitude and PF separate into three clusters. CL-1 has a peak frequency in the range of 15–132 kHz. CL-2 has a slightly higher peak frequency in the range of 133–328 kHz. CL-3 has a peak frequency over 329 kHz. For data for specimen type D shown in Fig. 6c, CL-1 has a peak frequency in the range of 15–154 kHz. CL-2 has a peak frequency in the range of 156–419 kHz, CL-3 has a peak frequency in the range of 421–996 kHz. Table 1 shows the cluster bounds of each type of specimen and the number of AE signals.

Obviously, the peak frequency of each cluster for specimens type C and D are higher than that for specimen B. This result shows that unlike the instantaneous failure of specimen of type B, the existence of the off-axis angle morphology makes the specimen progressively fail, and the long failure duration also affects the characteristics of the AE signals. It is found that the peak frequency of each cluster for data from specimen type D is higher than that for specimen type C. Meanwhile, based on the results seen with previous research [14, 16, 31, 32], CL-1 is likely related to the matrix cracking mode. With the aggravation of the damage degree, the fiber debonding which is likely represented by C-2 occurs in the composites. Before reaching the failure loading, fiber breakage damage which is likely represented by C-3 appears in the composites.

Besides analysis of the loading process as a whole, it can be divided into two stages for further study. For specimen type B, the first stage is defined as from 0 to 10 kN, and the second stage is defined as from 10 kN to 29.3 kN (failure load). When the load reached 5.4 kN, the specimen type D
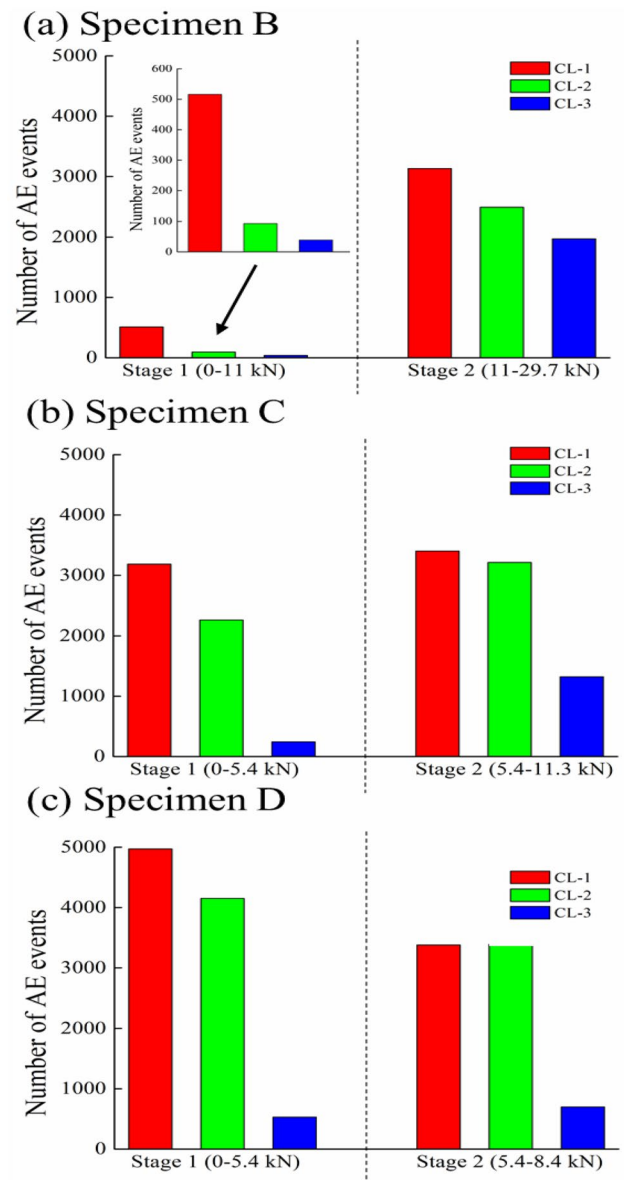

Fig. 7 Distribution of the AE signals in different stages for **a** specimen B, **b** specimen C and **c** specimen D, respectively (Color figure online)

Table 1 Cluster bounds of each type of specimen and the number of AE signals

	Specimen B		Specimen C		Specimen D	
	PF/kHz	Number	PF/kHz	Number	PF/kHz	Number
CL-1	13–105	3645	15–132	6591	15–154	8351
CL-2	107–189	2588	133–328	5478	156–419	7541
CL-3	191–466	2009	329–855	1569	421–996	1229

appeared to have significant deformation which could be clearly seen, so 0 to 5.4kN is defined as the first stage for both specimen type C and D; from 5.4kN to failure (11.3kN for specimen type C and 8.4kN for specimen type D) is defined as the second stage. The AE signals collected from the corresponding parts of the loading process were statistically analyzed.

The distribution of the AE signals in different stages for specimen type B, C and D were analyzed. For the data for specimen type B as shown in Fig. 7a, for the first stage, the number of AE signals is relatively small, which indicates that there is almost no damage in the specimen. In the second stage, the rate of AE signal increases for all the three clusters significantly which means all three kinds of damage begin to generate. Nevertheless, for specimen type C, with data as shown in Fig. 7c, at the first stage, the number of cluster CL-1 and CL-2 are large, which means in this stage damage is already developing and the main damage appears to be matrix cracking and fiber debonding. While there are a limited number of AE events for CL-3, which represents the condition when there are limited fiber broken. For the data for the second stage of specimen type C, the number of cluster CL-3 obviously goes up, which means a significant number of fiber breakage occurs besides matrix cracking and fiber debonding. It is similar for specimen type D for the first stage as shown in Fig. 7d. However, compared to data for specimen type C, there are obviously more events for all CL-1, CL-2 and CL-3, which means there is more damage developing in specimen type D at the first stage. However, for the second stage there are fewer events in CL-3 compared to specimen type C while there are more events for CL-1 and CL-2. This means that for the second stage, there are more fiber breaks occurred for specimen type C, as compared to specimen type D, and there is less matrix cracking and fiber debonding occurring.

3.4 Progressive Damage Analysis Based on Micro-CT

Micro-CT can be used to monitor the internal damage modes of CFRP laminates at the microstructure level, which can be used to investigate the progressive damage analysis and material capability [17–20].

To characterize and compare the damage occurring in the specimens, Micro-CT imaging was performed after the first stage for specimens of type C and D, and examples of the data are shown in Fig. 8.

In Fig. 8a, the 3-D part of specimen type C that been analyzed by Micro-CT is shown and the red rectangular box provides a vertical slice taken near the middle of the sample. The enlarged 2-D image is also shown. These images show that there is no obvious deformation. Corresponding data for specimen type D are shown in Fig. 8b. It is seen that a small number of fibers inside the specimen type D break along the off-axis angle direction and the surface deforms.

In order to further study the internal damage occurring in the specimens type C and D, Micro-CT imaging was performed on the cross sections of the specimens at different positions at the edges of 1/4, 1/3, and 1/2 where there deformation can be seen visually. The tomographic cross-sections images of specimens type C and D at the different positions are shown in the Figs. 9 and 10.
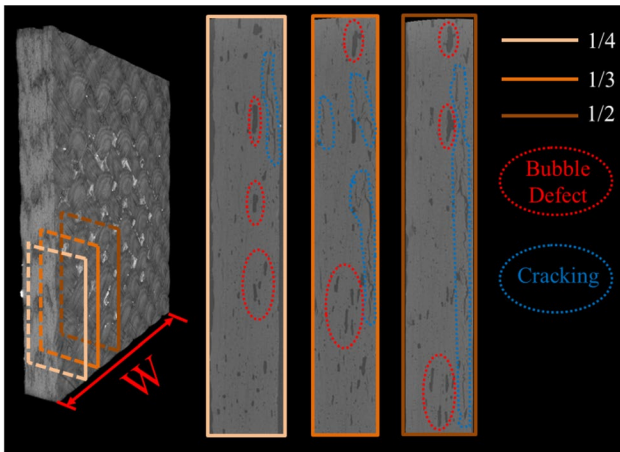
For specimen type C in Fig. 9, it could be seen that in the cross section there are some void/bubble defects, which most probably is due to matrix cracking and fiber debonding
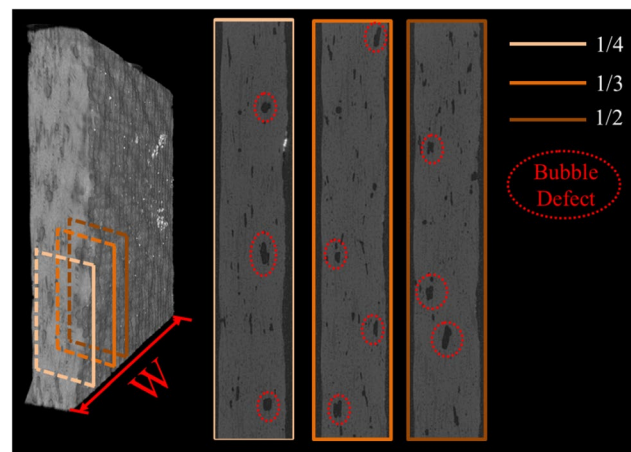
Fig. 9 The tomographic cross-sections images of specimen type C at different positions for the first stage

Fig. 8 Tomographic frontal morphology images of **a** specimen C and **b** specimen D
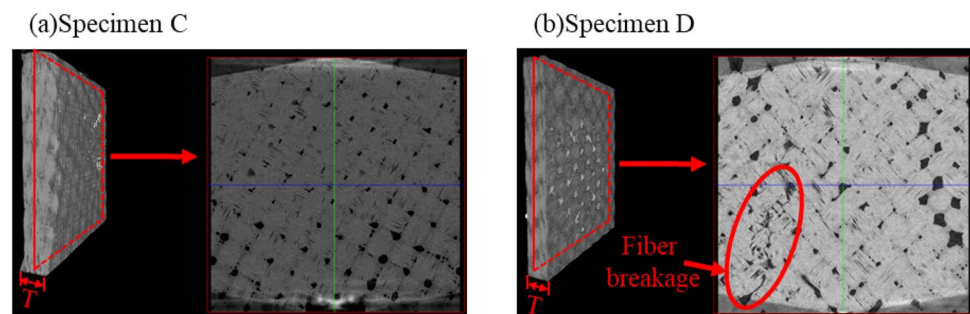
Fig. 10 The tomographic cross-sections images of specimen type D at different positions for the first stage (Color figure online)

damage. These types of damage are, consistent with the cluster analysis result of AE signal processing for the first stage of specimen type C shown in Fig. 7b.

For specimen type D shown in Fig. 10, there are not only some void/bubble defects but also small cracks which most probably are due to fiber breakage. This type of damage is consistent with the cluster analysis result of AE signal for

the first stage of specimen type D shown in Fig. 7c. In comparing the images in Figs. 9 and 10, it appears that specimen type C has a higher load capacity than specimen type D.

The morphology for the front face of the sample and cross-section images of specimen type C after the second stage loading are shown in Fig. 11. It can be seen in the cross-sectional images that for the damage locations and the morphology for the different cross sections, multiple damage modes such as matrix cracking, fiber debonding and fiber breakage have all occurred. From observing the cross-section damage image, it can be seen that under the condition of uniform force, the location of the obvious damage is consistent with the off-axis angle. It can be also observed that when the failure occurred, the specimen did not break along a line in the structure due to the off-axis angle structure.

The frontal morphology and cross-sections image of specimen type D after the second stage is also shown in Fig. 12. Compared with the image for specimen type C, the damage area for the specimen is much larger. The analysis shows that for specimen type C, multiple damage modes such as matrix cracking, fiber debonding and fiber breakage all have occurred. It can also be seen that from the frontal morphology that the specimen undergoes significant overall deformation. The reason for this appears to be is that the 45-degree off-axis angle causes the fibers in the
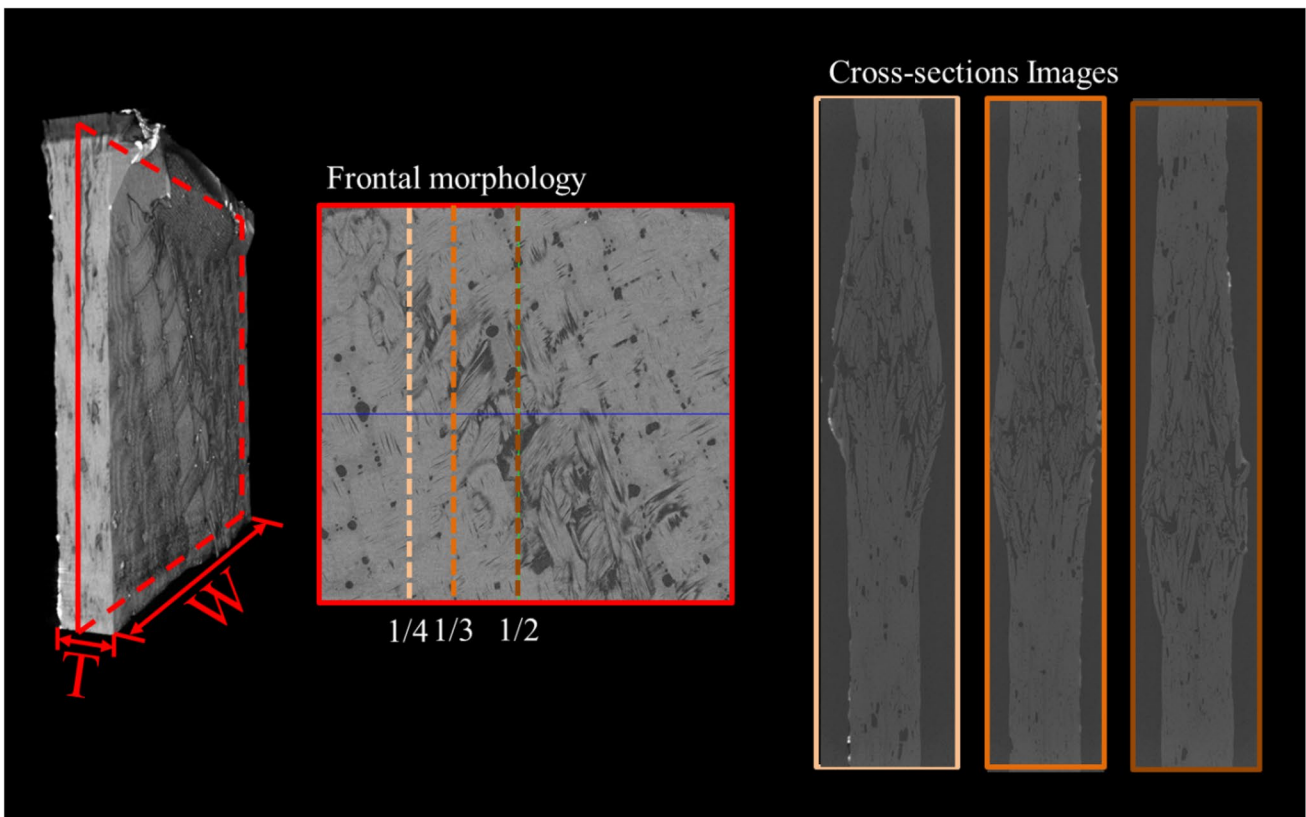
Fig. 11 The detailed information of the frontal morphology and cross-sections images of failed specimen C for the second stage

Fig. 12 The detailed information of the frontal morphology and cross-sections images of failed specimen D for the second stage
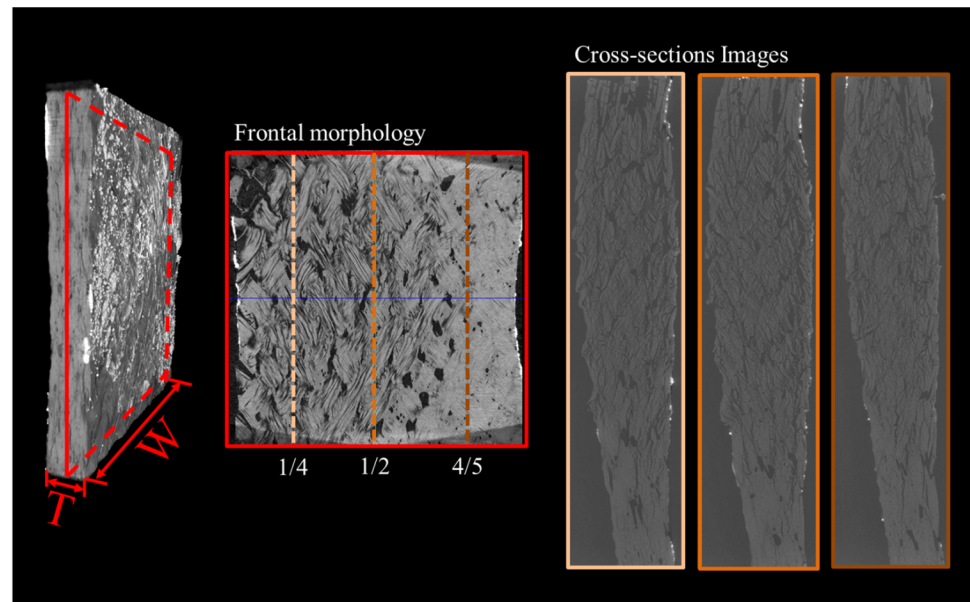
two directions of orthogonal weaving to be simultaneously stressed, resulting in the overall failure of the specimen and symmetrical deformation. With the off-axis angle, the specimen did not have fracture damage, which provides evidence that off-axis angle designs can enhance the toughness of the specimen. This finding appears to support one obvious advantage of the use of off-axis structural angles. When comparing images in Figs. 11 and 12, it can seen that there is a larger damage area for specimen type D as compared to specimen type C. This is a difference in process, which can lead to more cumulative hits numbers with AE data, although this is a qualitative rather than quantitative finding.

From the observations which form the basis for the discussion above, it appears that the damage seen and characterized with Micro-CT imaging can be correlated with damage regimens and phenomena characteristics as seen in the analysis of the AE signals. In other words, Micro-CT imaging and AE signals have a certain degree of complementarity.

4 Conclusions

In this work, progressive tensile tests for carbon fiber composites containing MWCNTs with different off-axis orientation angles were monitored by AE technology and viewed using a micro-CT system. Some important conclusions are:

1. The results show that the addition of MWCNTs can improve the bearing capacity of the composite and the off-axis angle configuration can enhance the toughness of the composite.
2. The AE signals collected during the tensile testing were post processed using a FCM algorithm and dis-

tinct groupings were observed. The groups seen with FCM analysis, appear to correlate with different damage mechanisms in the composite material, and these can be identified as matrix cracking, fiber debonding and fiber breakage. The characters of different AE signals are also shown, including how the frequency range for different kinds of damage can be identified, and these observations can potentially offer guidance for field applications of AE based SHM.

3. The off-axis material internal morphology can improve the toughness with the loss of stiffness and the ultimate tensile strength. Improvement in toughness can increase the load required for specimen break and enhance the safety level when the materials are deployed. It therefore appears that the use of such off-axis structure has advantages for industrial applications during the application of an external force.
4. For the loading test, the specimen with off-axis structure of 30° has better performance than that for off-axis of 45°. The off-axis structure with an angle of 45° has the ability to respond to large deformation while the main deformation along the fiber direction for the 30° off-axis circumstance. It was also found that the off-axis structure of 45° supports lower tensile load.
5. The micro-CT imaging of the composite specimen subjected to tensile loading can find the location of the internal damage of the composite. It is shown to be a good tool for analyzing damage evolution of composite materials. There is seen to be a good correlation between the damage seen with the Micro-CT imaging, the mechanisms identified and the data grouped with the AE signals that were post-processed by FCM. The data appears to demonstrated and validate the potential for

using AE monitoring signal with these classes of material. Combining AE technologies with micro-CT generated image analysis system can provide reference data for better understanding of phenomena occurring when monitoring the damage process and predicting failure.

The insights gained in the current work have implications that should be considered when looking to use multi-walled carbon nanotubes (MWCNTs) in the design of composite structures in the areas of aerospace, construction, and automotive applications.

References

1. Katnam, K.B., Da Silva, L.F.M., Young, T.M.: Bonded repair of composite aircraft structures: a review of scientific challenges and opportunities. Progr. Aerospace Sci. **61**, 26–42 (2013)

2. McCrory, J.P., Al-Jumaili, S.K., Crivelli, D., et al.: Damage classification in carbon fibre composites using acoustic emission: a comparison of three techniques. Composites B **68**, 424–430 (2015)

3. Ghadami, F., Dadfar, M.R., Zeraati, A.S.: Mixed mode I/II delamination analysis of rubber-modified glass-reinforced epoxy composites. J. Reinf. Plast. Compos. **33**(17), 1634–1643 (2014)

4. Tarfaoui, M., El Moumen, A., Lafdi, K.: Progressive damage modeling in carbon fibers/carbon nanotubes reinforced polymer composites. Composites B **112**, 185–195 (2017)

5. Kumar, D., Singh, K.K., Zitoune, R.: Impact of the carbon nanotube reinforcement in glass/epoxy polymeric nanocomposite on the quality of fiber laser drilling. Proc. Inst. Mech. Eng. B **232**(14), 2533–2546 (2018)

6. Khashaba, U.A., Aljinaidi, A.A., Hamed, M.A.: Analysis of adhesively bonded CFRE composite scarf joints modified with MWCNTs. Composites A **71**, 59–71 (2015)

7. Tarfaoui, M., El Moumen, A., Lafdi, K., et al.: Inter laminar failure behavior in laminate carbon nanotubes-based polymer composites. J. Compos. Mater. **52**(26), 3655–3667 (2018)

8. El Moumen, A., Tarfaoui, M., Lafdi, K.: Mechanical characterization of carbon nanotubes based polymer composites using indentation tests. Composites B **114**, 1–7 (2017)

9. Fotouhi, M., Najafabadi, M.A.: Investigation of the mixed-mode delamination in polymer-matrix composites using acoustic emission technique. J. Reinf. Plast. Compos. **33**(19), 1767–1782 (2014)

10. Saeedifar, M., Fotouhi, M., Najafabadi, M.A., et al.: Prediction of quasi-static delamination onset and growth in laminated composites by acoustic emission. Composites B **85**, 113–122 (2016)

11. Nikbakht, M., Yousefi, J., Hosseini-Toudeshky, H., et al.: Delamination evaluation of composite laminates with different interface fiber orientations using acoustic emission features and micro visualization. Composites B **113**, 185–196 (2017)

12. Njuhovic, E., Bräu, M., Wolff-Fabris, F., et al.: Identification of interface failure mechanisms of metal. Composites B **66**, 443–452 (2014)

13. Munoz, V., Vales, B., Perrin, M.: Damage detection in CFRP by coupling acoustic emission and infrared thermography. Composites B **85**, 68–75 (2016)

14. Li, L., Swolfs, Y., Straumit, I.: Cluster analysis of acoustic emission signals for 2D and 3D woven carbon fiber/epoxy composites. J. Compos. Mater. **50**(14), 1921–1935 (2016)

15. Arthur, M., Abderrahim, E.M., Zouhaier, J., et al.: Mechanical behaviour and damage mechanisms analysis of a flax-fiber reinforced composite by acoustic emission. Composites A **90**, 100–110 (2016)

16. Zhao, W.Z., Zhou, W.: Cluster analysis of acoustic emission signals and tensile deformation properties of carbon/glass fiber reinforced hybrid woven composites. Struct. Health Monit. Int J. **18**(5–6), 1686–1697 (2019)

17. Wang, Y., Burnett, T.L., Chai, Y., et al.: X-ray computed tomography study of kink bands in unidirectional composites. Compos. Struct. **160**, 917–924 (2017)

18. Tan, K., Watanabe, N., Iwahori, Y.: X-ray radiography and micro-computed tomography examination of damage characteristics in stitched composites subjected to impact loading. Composites B **42**, 874–884 (2011)

19. Madra, A., El Hajj, N., Benzeggagh, M.: X-ray micro-tomography applications for quantitative and qualitative analysis of porosity in woven glass fiber reinforced thermoplastic. Compos. Sci. Technol. **95**, 50–58 (2014)

20. Zhang, D.T., Liu, X.D., Gu, Y.H., et al.: Effects of off-axis angle on shear progressive damage of 3D woven composites with X-ray micro-computed tomography. Composites A **115**, 311–320 (2018)

21. Li, Z.X., Guo, L.C., Zhang, L., et al.: In situ experimental investigation on the out-plane damage evolution of 3D woven carbon-fiber reinforced composites. Compos. Sci. Technol. **162**(162), 101–109 (2018)

22. El Moumen, A., Tarfaoui, M., Lafdi, K.: Computational homogenization of mechanical propertiesfor laminate composites reinforced with thin film made of carbon nanotubes. Appl. Compos. Mater. **25**, 569–588 (2018)

23. Tarfaoui, M., Lafdi, K., El Moumen, A.: Mechanical properties of carbon nanotubes based polymer composites. Composites B **103**, 113–121 (2016)

24. El Moumen, A., Tarfaoui, M., Hassoon, O., et al.: Experimental study and numerical modelling of low velocity impact on laminated composite reinforced with thin film made of carbon nanotubes. Appl. Compos. Mater. **25**(2), 309–320 (2018)

25. Tas, H., Soykok, I.F.: Effects of carbon nanotube inclusion into the carbon fiber reinforced laminated composites on flexural stiffness: A numerical and theoretical study. Composites B **159**, 44–52 (2019)

26. Tarfaoui, M., El-Moumen, A., Lafdi, K.: Progressive damage modeling in carbon fibers/carbon nanotubes reinforced polymer composites. Composites B **112**, 185–195 (2017)

27. Cannon, R.L., Dave, J.V., Bezdek, J.C.: Efficient implementation of the fuzzy c-means clustering algorithms. IEEE Trans. Pattern Anal. Mach. Intell. **8**(2), 248–255 (1986)

28. Sun, H.J., Wang, S.R., Jiang, Q.S.: FCM-based model selection algorithms for determining the number of clusters. Pattern Recognit. **37**(10), 2027–2037 (2004)

29. Scanavini, A., Moscatti, M.: Computed tomography. In: Ahmad, A., Bond, L.J. (eds.) ASM Handbook, vol. 17, pp. 440–474. Materials Park, ASM International (2008)

30. Ahsan, A., Kryukov, I., Böhm, S.: Laser surface structuring of cemented carbide for improving the strength of induction brazed joints. J. Manuf. Mater. Process. **3**(2), 44 (2019)

31. Li, L., Lomov, S.V., Yan, X.: Cluster analysis of acoustic emission signals for 2D and 3D woven glass/epoxy composites. Compos. Struct. **116**, 286–299 (2014)

32. Zhou, W., Zhao, W.Z., Zhang, Y.N., et al.: Cluster analysis of acoustic emission signals and deformation measurement for delaminated glass fiber epoxy composites. Compos. Struct. **195**, 349–358 (2018)